Inorganic Chemistry

pubs.acs.org/IC

Article

Evolution of the Local Structure in the Sol–Gel Synthesis of Fe_3C Nanostructures

Matthew S. Chambers,* Dean S. Keeble, Dean Fletcher, Joseph A. Hriljac, and Zoe Schnepp*

Cite This: *Inorg. Chem.* 2021, 60, 7062–7069

Read Online

ACCESS | Metrics & More | Article Recommendations | Supporting Information

ABSTRACT: The sol–gel synthesis of iron carbide (Fe_3C) nanoparticles proceeds through multiple intermediate crystalline phases, including iron oxide (FeO_x) and iron nitride (Fe_3N). The control of particle size is challenging, and most methods produce polydisperse Fe_3C nanoparticles of 20–100 nm in diameter. Given the wide range of applications of Fe_3C nanoparticles, it is essential that we understand the evolution of the system during the synthesis. Here, we report an *in situ* synchrotron total scattering study of the formation of Fe_3C from gelatin and iron nitrate sol–gel precursors. A pair distribution function analysis reveals a dramatic increase in local ordering between 300 and 350 °C, indicating rapid nucleation and growth of iron oxide nanoparticles. The oxide intermediate remains stable until the emergence of Fe_3N at 600 °C. Structural refinement of the high-temperature data revealed local distortion of the NFe_6 octahedra, resulting in a change in the twist angle suggestive of a carbonitride intermediate. This work demonstrates the importance of intermediate phases in controlling the particle size of a sol–gel product. It is also, to the best of our knowledge, the first example of *in situ* total scattering analysis of a sol–gel system.

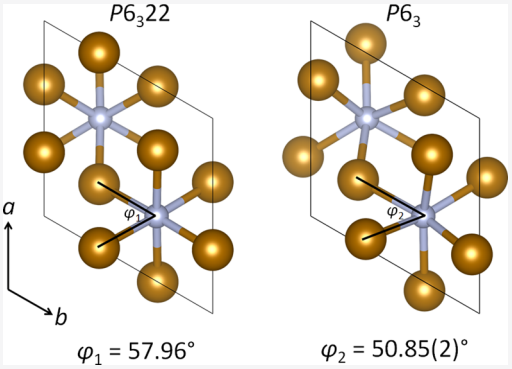

1. INTRODUCTION

Iron forms a range of interstitial compounds with carbon and nitrogen, including ε-Fe_3N and θ-Fe_3C (Figure 1). These have been widely studied due to their importance in steel but are now receiving renewed attention for their potential as catalysts. Iron nitrides and carbides have been used as catalysts in the Fisher–Tropsch process,[1,2] oxygen reduction reaction,[3] and ammonia decomposition.[4] Most recently, iron carbides and nitrides are being pursued due to their potential to replace rare and costly precious metals such as Pt in applications such as fuel cells.[5] Additionally, θ-Fe_3C (Fe_3C) and ε-Fe_3N (Fe_3N) have interesting magnetic properties and uses in biomedical applications.[6−8]

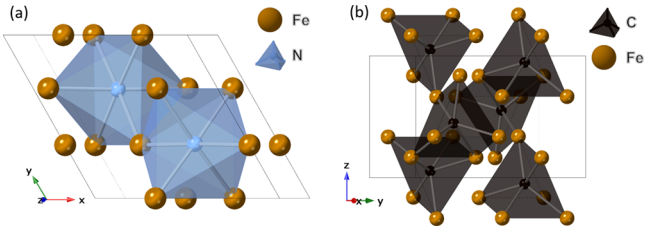

Figure 1. Crystal structures of (a) ε-Fe_3N and (b) θ-Fe_3C.

In order to fully exploit the potential of Fe_3N and Fe_3C, it is important to have controlled routes to nanoparticles of these materials.[7] Various routes have been proposed to achieve this goal, including laser ablation, ammonolysis of iron oxide nanoparticles, nanocasting,[9] solvothermal synthesis[8,10] and sol–gel chemistry. Sol–gel chemistry has the advantage of being relatively simple both in terms of the precursors and processing. In general, sol–gel synthesis of Fe_3N or Fe_3C nanoparticles is achieved by mixing aqueous iron salts (e.g., nitrate and acetate) with organic molecules such as urea[11] or gelatin[12] as well as with CTAB and melamine.[7] The resulting "gel" is dried and pyrolyzed in an inert atmosphere to produce nanoparticles of the required product. While sol–gel chemistry is simple and scalable, it is difficult to achieve significant control over the particle size. It is also difficult to isolate pure nitride or carbide phases and small changes in experimental conditions can have a large effect on the product composition (Fe_3N/Fe_3C/Fe).[13] In order to maximize the beneficial catalytic properties of iron nitrides and carbides and fully explore their potential, it is essential to gain a better understanding of how they are formed.

In *in situ* synchrotron X-ray diffraction studies, we showed that the sol–gel route to Fe_3C proceeds via several

Received: December 17, 2020
Published: May 4, 2021

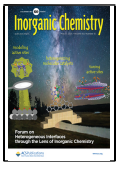

intermediates (Scheme 1).[12] In a system involving gelatin and iron nitrate as precursors, the reaction was shown to proceed via an intermediate iron oxide phase. Significant peak broadening suggested that the particle diameter in this phase was very small (estimated at ~3 nm). This is consistent with transmission electron microscopy (TEM) images that show iron oxide nanoparticles embedded in a carbon matrix. From 560 °C, sharp Fe_3N peaks emerged and from 610 °C, sharp Fe_3C peaks were observed, produced by carbothermal reduction and nitridation of the iron oxide intermediate by the surrounding nitrogen-doped carbon matrix. The Scherrer analysis indicated larger crystallite diameters of 30 nm (Fe_3N) and 60 nm (Fe_3C), again consistent with the TEM images. The Fe_3N to Fe_3C transition was believed to proceed via carbon diffusion into the nitride (forming a carbonitride intermediate), based on observations of a peak shift in the Fe_3N phase.

Scheme 1. Proposed Reaction Mechanism for Fe_3C Formation

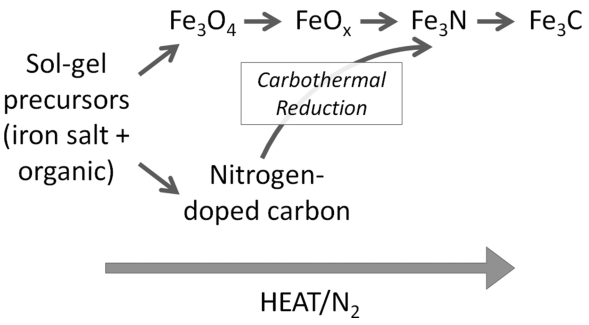

We now report an *in situ* synchrotron total scattering study of the sol–gel synthesis of Fe_3C. Total scattering and the pair distribution function (PDF) have been widely used *ex situ* to study the local order in crystalline and amorphous materials. They have also been used *in situ* to study nanoparticles formed in solvo/hydrothermal synthesis, showing the evolution of local and long-range structures.[14,15] These systems, however, are comparatively simple as they involve only two or three precursor phases that evolve to a single phase suspended in a solvent. Total scattering has enormous potential to aid the understanding of sol–gel synthesis of materials. It offers information about local structural details that may be missed in Bragg scattering. It also allows us to examine the evolution of

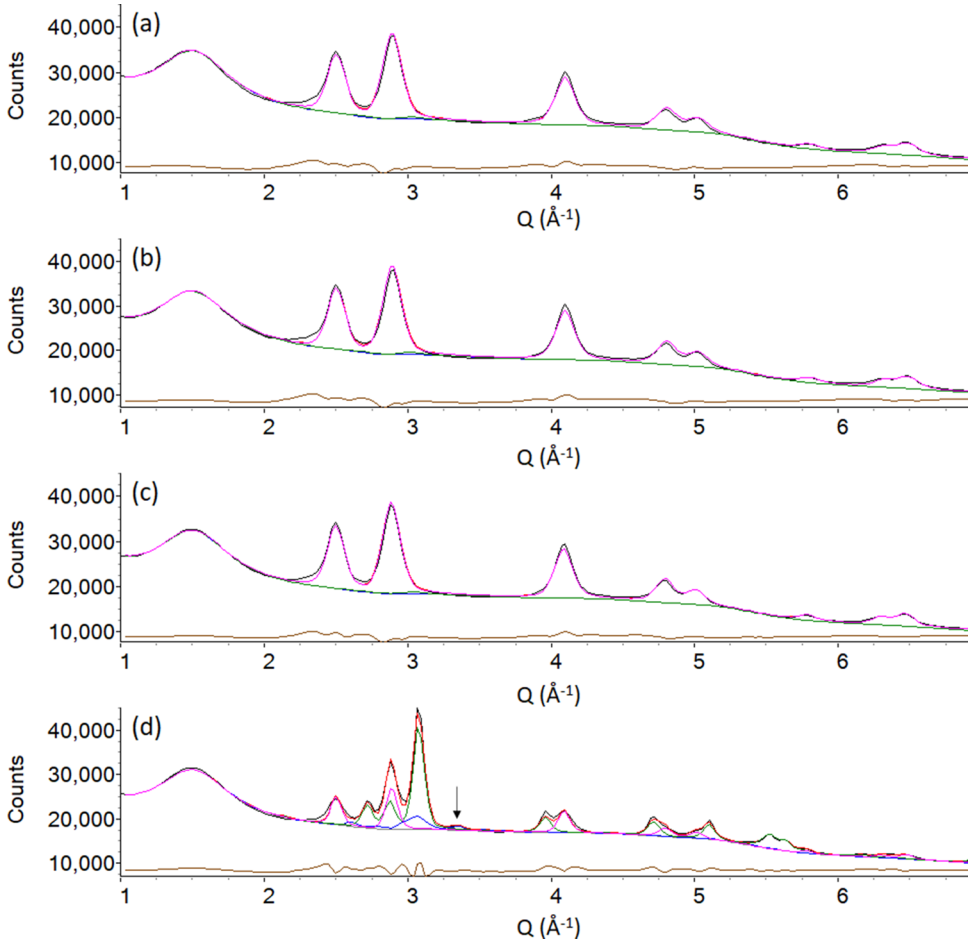

Figure 2. Rietveld plots from the *in situ* $Fe(NO_3)_3$/gelatin sol–gel reaction, (a) T = 350 °C, R_{wp} = 1.605%; (b) T = 400 °C, R_{wp} = 1.729%; (c) T = 500 °C, R_{wp} = 1.382%; and (d) T = 600 °C, R_{wp} = 1.602%. The black curves represent the observed data, the red curves the total calculated pattern, the brown curves are the difference between observed and calculated pattern, the pink curves the calculated pattern arising from FeO_x, the green curves the calculated pattern arising from Fe_3N, the blue curves represent the pattern arising from Fe_3C, and the gray curves are the background. In panels (a–c), Fe_3C and Fe_3N were included in the refinements to ensure trace amounts were not missed but contribute 0% to the calculated pattern. The peak in panel (d) highlighted with the black arrow arises from Fe_3C.

https://doi.org/10.1021/acs.inorgchem.0c03692
Inorg. Chem. 2021, 60, 7062–7069

particle size and crystallinity at lower temperatures where no long-range order is present. The data in this study specifically demonstrate the very fast crystallization of the iron oxide intermediate during Fe_3C synthesis. It also offers insight into the formation and structure of the Fe_3N intermediate. To the best of our knowledge, this study is the first example of an *in situ* total scattering study of a sol−gel process. This is particularly significant as it shows that PDF analysis can be used to extract useful information from complex systems where there are multiple crystalline and amorphous components.

2. EXPERIMENTAL PROCEDURE

2.1. Synthesis. The synthesis of the gelatin precursor was performed as described in the previous literature.[12] A hot aqueous solution of gelatin (10%, w/w, 10 g, Sigma-Aldrich, G2500) with aqueous iron nitrate (10%, w/v, 20.2 mL, $Fe(NO_3)_3{\cdot}9H_2O$) formed a viscous orange gel. The orange gel was dried in air at 70 °C to produce a brittle orange-brown foam.

2.2. X-ray Total Scattering. X-ray total scattering data were collected using a wavelength of $\lambda = 0.16167$ Å. Samples of the orange-brown foam were ground and loaded into 1 mm diameter fused silica capillaries (with one end sealed) at the Diamond Light Source beamline I15-1. A hot air blower was used for the variable temperature experiments, and pure N_2 was blown over the open end of the capillary to prevent oxidation of the sample. A temperature calibration was performed using a Si-Al_2O_3 standard.[16] Data were collected from 150 to 400 °C in 50 °C increments and at 500 and 600 °C, with a heat rate of 10 °C min^{-1}. Each data collection was 10 min in length. During heating, the samples underwent expansion due to the release of gases from gelatin decomposition, so the samples were occasionally repacked with a thin wire.

2.3. Rietveld Refinement. Rietveld refinements were performed using TOPAS v6.[17,18] The starting models were derived from the following sources: FeO_x (refined with the fixed stoichiometry of FeO) from Fjellvåg *et al.*,[19] Fe_3C from Wood *et al.*,[20] and Fe_3N from Jacobs *et al.*[21] Backgrounds were described using sixth-order Chebyshev polynomials and with the scans of the empty fused silica capillaries collected at similar temperatures, where a refined scale factor was included. Peak shapes were described using the Thompson−Cox−Hastings pseudo-Voight function. Additionally, a zero-point parameter was refined. A range of $1.5 \leq 2\theta \leq 20°$ was used. Refinements were performed against Bragg scattering obtained from the total scattering experiments described above for temperatures of 350, 400, 450, 500, and 600 °C. Attempts to perform Rietveld refinements against the data for 200−300 °C were made, but it was found that the entirety of the Bragg scattering can be described by the empty capillary backgrounds (Figure S1, Supporting Information). As the sample at 200 °C showed no Bragg scattering, no Rietveld analysis was attempted at 150 °C.

2.4. Small-Box PDF Refinements. Small-box PDF refinements were performed using TOPAS v6.[22] The PDF data were obtained using GudrunX[23] version 5 to produce $D(r)$ data (as defined by Keen).[24] The $D(r)$ data were produced using $Q_{max} = 20$ Å^{-1}. A Lorch[25] correction function was used to remove Fourier ripples generated from the limited Q_{max}. The broadening power of the function was set to 0.03 Å. For the refinement performed against the 600 °C data, the same phases used in the Rietveld refinement were included in the PDF refinements. Additionally, two amorphous carbon phases were modeled using graphite (starting model obtained from Trucano and Chen)[26] for sp^2 carbon and diamond (starting model obtained from Yamanaka and Morimoto)[27] to model sp^3 carbon. A function available in TOPAS[22] that removes correlations at ranges of $r = 5$ Å was applied to these phases to model them as amorphous. Additionally, a further Fe_3N phase with symmetry lowered from $P6_322$ to $P6_3$ was included. The $P6_3$ phase was limited to contributing to the PDF at r <4.1 Å, while $P6_322$ was limited to contributing at r >4.1 Å to simulate local ordering.

3. RESULTS AND DISCUSSION

3.1. Rietveld Analysis. The data from 200 to 300 °C produced negligible Bragg scattering and so were fitted using only the empty capillary background (Figure S1). For data collected from 350 to 600 °C, Rietveld analysis was used in order to estimate the compositions of crystalline components to produce the PDF data. Figure 2, showing the observed data and Rietveld plots, shows that for $350 \leq T \leq 500$ °C, there is a very little change in the composition of the sample. FeO_x (wüstite) is the only crystalline phase present and the broad peaks (indicative of a small crystallite size) are consistent with the previous synchrotron diffraction data.[12] At $T = 600$ °C, there is a dramatic change in the pattern where Fe_3N becomes the major phase, with some FeO_x still present and Fe_3C beginning to form. Several peaks that arise from Fe_3C are in similar positions to those that are from Fe_3N, which can potentially result in Rietveld refinement software fitting the background using the structural parameters of Fe_3C. Despite the weak intensity arising from Fe_3C, there is evidence to suggest the presence of crystalline Fe_3C. The peak at $Q = 3.3$ Å^{-1} arises from Fe_3C and is unaccounted for in refinements where Fe_3C was excluded. Additionally, our previous *in situ* synchrotron diffraction experiment,[12] which was performed using a high Bragg resolution instrument, also showed Fe_3C beginning to form at 600 °C. The calculated weight percentages for FeO_x, Fe_3N, and Fe_3C are approximately 29, 48, and 22%, respectively. It is likely that the calculated weight percentage for Fe_3C is higher than the real weight percentage. The "excess" Fe_3C that is calculated here is calculated at the expense of Fe_3N due to the large overlap of potential Bragg peaks. However, for the purpose of this study, which was to obtain an approximate composition for processing the PDF data, the effect is negligible. This is due to the very similar X-ray scattering lengths and densities of Fe_3N and Fe_3C. The peaks arising from Fe_3N are also far more noticeable than those from Fe_3C due to the higher symmetry of Fe_3N ($P6_322$ compared to *Pnma*). The peak sharpness also indicates that the Fe_3N phase is more crystalline and has bigger particles than the FeO_x phase.[28,29] The synchrotron XRD experiment showed Fe_3O_4 at low temperatures, which is not observed in this new data, presumably due to the longer scan times (i.e., periods of thermal equilibrium) required for collecting data of sufficient quality for PDF analysis. Indeed, our previous laboratory studies have also shown that the onset point of the Fe_3O_4 to FeO_x transition is dependent on experimental conditions.[13] It is also possible that the experimental setup (N_2 gas flowing over the end of a closed capillary as opposed to through the capillary via a retort) caused this slight variation in the system.

As Bragg scattering can only be produced by materials with a long-range order (i.e., crystalline materials), it cannot tell us about the nature of any amorphous phases present. However, as carbon is likely to make up most of the amorphous fraction of the sample, the contribution of the amorphous phases to the total scattering factor will be negligible compared to the much more electron-dense crystalline iron compounds. Therefore, the phase compositions extracted from the Rietveld refinements represent a good approximation for use in the total scattering processing to produce the PDFs.

3.2. PDF Analysis. In order to probe the local structure, the PDFs from 150 to 600 °C were produced. Due to the similar peak positions and X-ray scattering of Fe_3C and Fe_3N, we also processed the data using Rietveld refinements where

https://doi.org/10.1021/acs.inorgchem.0c03692
Inorg. Chem. 2021, 60, 7062−7069

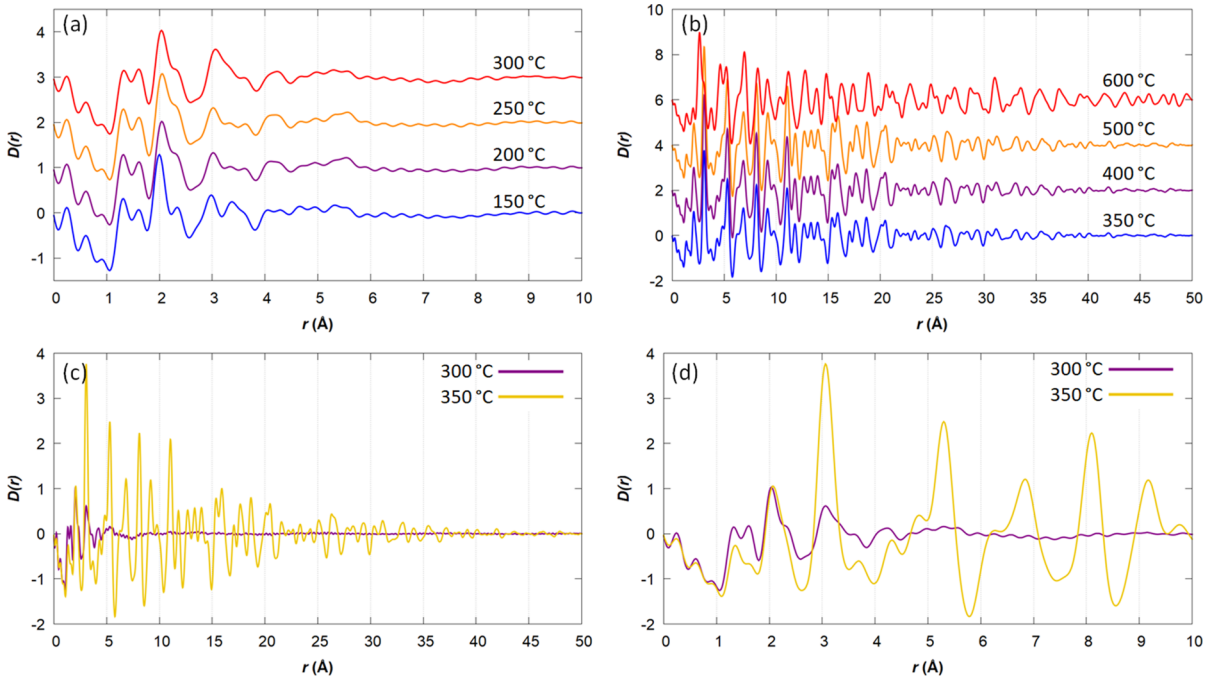

Figure 3. PDFs of the $Fe(NO_3)_3$/gelatin sol−gel reaction obtained at (a) T = 150−300 °C, (b) T = 350−600 °C, and T = 300 °C vs 350 °C from (c) 0−50 Å and (d) 0−10 Å.

Fe_3C was excluded. The resultant PDFs at 600 °C were nearly identical (Figure S2), indicating that even if the Fe_3C composition has been overestimated this will not impact the conclusions from the PDF analysis. Figure 3a shows the PDFs obtained for samples from 150 to 300 °C. The data illustrate that the iron oxide phase, which is most likely to be Fe_3O_4 at this temperature, based on previous studies[12] has a very short-range order with no correlations above r = 6 Å. This is an even shorter range of order than is observed in amorphous carbon, which typically shows correlations in the range of $10 \leq r \leq 20$ Å.[30,31] Fe_3O_4 has been shown to produce highly crystalline nanoparticles when synthesized via a solution route, with correlations extending nearly through the entire nanoparticle.[32] The very short-range order in our system therefore suggests that the sample is completely amorphous up to 300 °C rather than containing very small crystalline iron oxide nucleation clusters. Sol−gel methods have for many years been promoted as routes that maximize homogeneity in solid-state precursors[33] and these PDF data are direct evidence that this is in fact the case.

Between 150 and 200 °C, there is a peak in the region of $2.0 \leq r \leq 2.6$ Å that shifts and broadens. This region corresponds to the average Fe−O distances in Fe_3O_4 (1.89 and 2.06 Å) and FeO_x (2.16 Å).[19,34] and the shift in the large peak from ∼2.0 to ∼2.1 Å suggests the carbothermal reduction of amorphous Fe_3O_4 to FeO_x. It is possible that the shift is due to the final decomposition of the iron nitrate precursor. However, there is also a further peak broadening from 250 to 300 °C at $3.0 \leq r \leq 3.8$ Å, corresponding to the first Fe−Fe distance in Fe_3O_4 and FeO_x, which provides further evidence that an amorphous Fe_3O_4 phase is being converted to FeO_x.

Figure 3b shows the PDFs in the temperature range of 350−600 °C, where the samples show Bragg scattering. The first thing that should be noted is the difference in scale. There is a dramatic change from 300 to 350 °C in a system that has a much higher range of order, with correlations that extend to >40 Å. This is highlighted in Figure 3c which shows the fast (5 min) transition from an amorphous material with a very short-range order at 300 °C to a material with clear crystalline regions at 350 °C. The transition is consistent with the emergence of Bragg peaks for FeO_x, showing the onset of crystallization of FeO_x nanoparticles from the amorphous precursor. The local structures at 300 and 350 °C are similar at <5 Å (Figure 3d), though the peaks are a lot sharper at 350 °C. This indicates that the change in the system is a structural rearrangement of the locally disordered iron oxide material into ordered domains rather than a chemical transition as there are atom pairs distributed at very similar values. The broader distributions found at 300 °C are likely due to the increased disorder compared to those at 350 °C, though there is a possibility of a small quantity of left over precursor materials. This reflects the similar observations that have been made in solution-state crystallization processes, such as the formation of amorphous NaCl clusters followed by a sudden onset of crystallization.[35]

An attempt was made to refine the local structure at 350 °C using FeO_x and an amorphous carbon phase. In this case, we used a refinement with FeO_x using its long-range symmetry (Fm-3m) and a graphite phase with correlations at r >5 Å removed. This was found to provide a better fit (Figure S3a, R_{wp} = 22.029% and χ^2 = 0.173) than with short-range diamond or a diamond/graphite combination. This fit was not satisfactory for r <4 Å, so another phase of FeO_x with a lower $P4$ symmetry was added to account for local breaking of symmetry (Figure S3b). Having a lower symmetry in the local structure while having a higher symmetry long-range structure due to disorder is commonly observed in oxide materials such as $Ba_2In_2O_5$ and $La_2Mo_2O_9$.[36,37] While this did improve the fit (R_{wp} = 19.150% and χ^2 = 0.151), there were still some discrepancies with the peak at r = 1.4 Å, corresponding to the carbon phases, and the peak at r = 2.1 Å, corresponding to the nearest neighbor Fe−O distance. FeO_x is known to have a

https://doi.org/10.1021/acs.inorgchem.0c03692
Inorg. Chem. 2021, 60, 7062−7069

highly defective (and often oxygen-deficient) structure containing Frenkel defects.[19] This fact, combined with the complexity of the overall system, means that there could be many factors contributing to peak broadening and shifting.

From 350 to 500 °C, there is a very little change in the PDF, suggesting that there is no significant growth in the FeO_x nanoparticles. Between 500 and 600 °C, there is another dramatic change, and in this case, there is a substantial shift in peak intensities and positions, correlating to the observation of Fe_3N peaks in the Bragg scattering. At 600 °C, there are correlations up to r = 50 Å, which is the maximum distance that the PDFs were processed to. This indicates a growth in the crystallite size during the FeO_x to Fe_3N transition.

In order to fully characterize the PDF data for the complex mixture of components present at 600 °C, structural refinements were performed for Fe_3C, Fe_3N, and FeO_x using TOPAS. The raw data and the resulting fit are shown in Figure 4. One challenge with the analysis was how to reasonably include the amorphous carbon component. TOPAS v6 can only include crystalline phases;[22] however, it also permits the use of functions that scale calculated contributions as an arbitrary function of distance. This allows amorphous phases with a very short-range order to be approximated. Therefore, both diamond and graphite were included in our refinement (with correlations for r >5 Å removed) to model the mixture of sp^2 and sp^3 carbons that result from the decomposition of gelatin.[38] The C−C distances found in sp^2 and sp^3 carbons range from 1.4 to 1.5 Å, corresponding to the first peak in the PDF at ∼1.42 Å. As the majority of the scattering is produced by the Fe-containing phases and the primary purpose of this study is the structure of the Fe_3N nanoparticles, we propose that this approximation for the carbon phase is sufficient. The cell parameters of all included phases were refined according to their long-range symmetry as well as spherical atomic displacement parameters. Atomic coordinates were only refined for Fe_3N as it was the primary phase, whereas Fe_3C constituted only an estimated 22% by weight of the sample at this temperature, so there was not enough sensitivity in the PDF to accurately refine the coordinates.

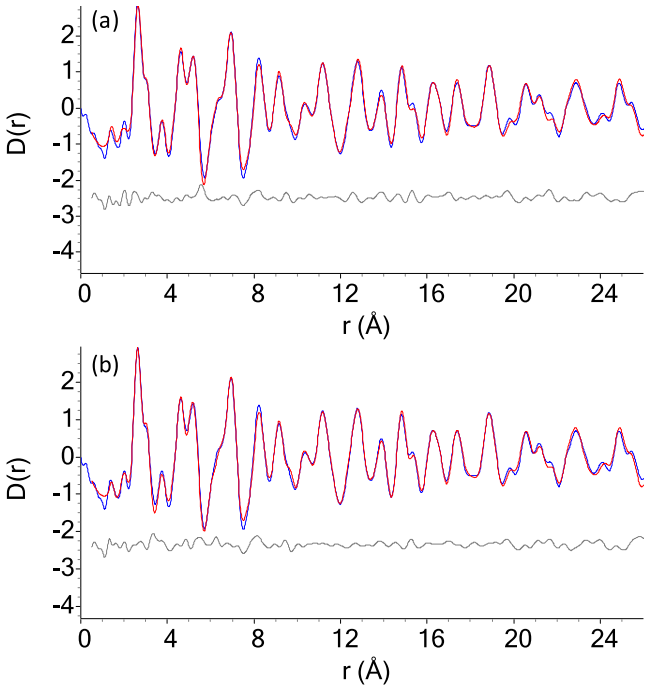

Figure 4. PDF refinements of the $Fe(NO_3)_3$/gelatin sol−gel reaction at 600 °C. (a) Refinement with FeO_x, Fe_3C, amorphous sp^2 and sp^3 carbon phases, and only $P6_322$ Fe_3N, R_{wp} = 12.318%, and χ^2 = 0.099; (b) refinement with FeO_x, Fe_3C, amorphous sp^2 and sp^3 carbon phases, and two phases of Fe_3N: one with $P6_3$ symmetry for r <5.0 Å and one with $P6_322$ for r >5.0 Å, R_{wp} = 11.629%, and χ^2 = 0.094. Blue curve = observed PDF and red curve = calculated PDF.

Initial refinements used a single phase of Fe_3N with its long-range space group of $P6_322$. While this resulted in a near-satisfactory fit (Figure 4a, R_{wp} = 12.318% and χ^2 = 0.099), the first two peaks, corresponding to the amorphous carbon phases and the nearest-neighbor Fe−N distance in Fe_3N, do not fit. They were instead shifted as a result of incorrect cell parameters. It is not uncommon for materials to locally break symmetry, such as in $Ba_2In_2O_5$ and $La_2Mo_2O_9$.[36,37] In order to address this, a lower-symmetry $P6_3$ phase of Fe_3N was used in addition to the $P6_322$ phase. The $P6_3$ space group is a maximal subgroup of $P6_322$, where the twofold rotational axes parallel and perpendicular to the x and y axes have been removed. This provides more degrees of freedom to the Fe atoms as they move from the 6g Wyckoff position [$(x, 0, 0)$] in the $P6_322$ phase to the general 6c Wyckoff position [(x, y, z)]. It also provides additional degrees of freedom to the N atoms as the z coordinate is allowed to be refined in the $P6_3$ phase (Tables 1 and 2). By refining with just the $P6_3$ phase, it was found that the optimal range for r to refine with the lower symmetry phase is r <5.0 Å. Thus, another refinement was performed including two phases of Fe_3N: a $P6_3$ phase contributing to the scattering at r <5.0 Å and a $P6_322$ phase contributing to the pattern at r >5.0 Å. This fit is shown in Figure 4b and resulted in better fitting of the positions of the first two peaks at r = 1.4 Å and r = 2.0 Å (R_{wp} = 11.629% and χ^2 = 0.094). There is some intensity in the calculated curve at r < r_{min}; this is due to TOPAS broadening the peak shape function.

Table 1. Structural Parameters of Fe_3N at 600 °C in the Space Group $P6_322$[a]

site label	Wyckoff site	x	y	z	occupancy
Fe1	6g	0.336(3)	0	0	1
N1	2c	$^1/_3$	$^2/_3$	$^1/_4$	1

[a]Cell parameters: a = 4.6271(7) Å, c = 4.3664(9) Å, α = 90°, γ = 120°, and V = 80.96(3) Å^3.

Table 2. Structural Parameters of Fe_3N at 600 °C in the Space Group $P6_3$[a]

site label	Wyckoff site	x	y	z	occupancy
Fe1	6c	0.326(3)	0.045(3)	0(2)	1
N1	2b	$^1/_3$	$^2/_3$	0.2(2)	1

[a]Cell parameters: a = 4.72(1) Å, c = 4.48(2) Å, α = 90°, γ = 120°, and V = 86.3(5) Å^3.

Due to the increased degrees of freedom of the Fe and N atoms, the twist angle of the NFe_6 octahedra is adjusted in the $P6_3$ phase. The twist angle, φ, is a parameter used in coordination chemistry to describe how trigonal-prismatic or octahedral in nature a sixfold coordinate polyhedron is, where φ = 0° is a perfect trigonal prism and φ = 60° is a perfect octahedron.[39,40] In the long-range order, the average structure

https://doi.org/10.1021/acs.inorgchem.0c03692
Inorg. Chem. 2021, 60, 7062−7069

of Fe_3N with a $P6_322$ symmetry, φ_1 = 57.96°,[21] is an almost perfect octahedron. The CFe_6 polyhedra in Fe_3C are trigonal prisms, so a gradual shift in the local structure could be expected if the nitride to carbide transformation occurs via gradual replacement of N atoms with C.[41,42] The twist angle in the $P6_3$ phase in our system was found to be φ_2 = 50.85(2)°. The difference between the two structures is illustrated in Figure 5. While the conformation is still primarily octahedral,

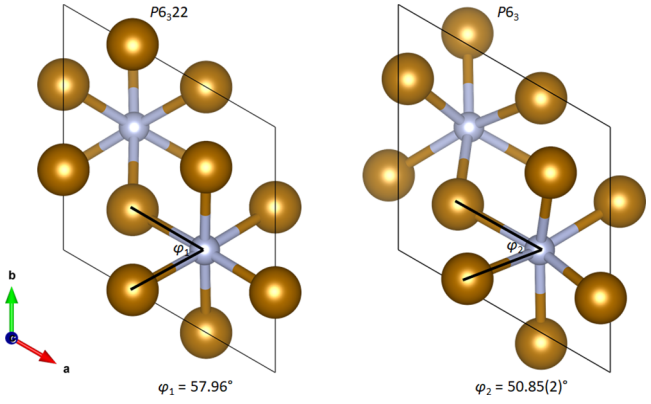

Figure 5. Twist angles obtained from Fe_3N in $P6_322$ at room temperature[21] and in $P6_3$ at 600 °C. Fe atoms are shown in gold and N in silver. The figure is a 2D projection and the angles shown do not include the z coordinates of the atoms.

the NFe_6 polyhedra are distorted and more trigonal prismatic in nature compared to the average structure. Given that iron carbonitride phases are known to exist,[12,43] it is plausible that the distortion in the octahedra could be due to the incorporation of C into the structure as Fe_3N reacts with the surrounding carbon during the formation of Fe_3C. A detailed *ex situ* total scattering study of these systems would be necessary to establish whether the distortion is indeed due to carbon diffusion or whether it is an intrinsic feature of Fe_3N. Distinguishing between carbon and nitrogen through atomic form factors alone is challenging in total scattering but is possible by comparing the bond lengths.

4. CONCLUSIONS

In situ total scattering has been used to probe the evolution of FeO_x and Fe_3N nanoparticles from a $Fe(NO_3)_3$/gelatin sol–gel precursor. Despite the complex, multicomponent nature of the system, we were able to extract valuable information about the intermediate phases and phase transitions. The onset of crystallization is very fast. Correlations in the PDFs are only observed at <6 Å at 300 °C, indicating a highly amorphous structure. At 350 °C, however, there are correlations up to ∼40 Å and this is only 5 min further on in the synthesis. This lack of change in the short-range order during this transition indicates that crystallization of FeO_x nanoparticles occurs from the local structural rearrangement of the atoms. Given that the size and nature of intermediate oxide phases in the sol–gel synthesis can dramatically affect the nature and morphology of a ceramic product,[44] this ability to observe early nucleation stages *in situ* could enable us to tune the synthesis conditions in our system to achieve more control over the particle size. Our results also offer insight into the Fe_3N phase. At 600 °C, when Fe_3N becomes the dominant phase, the nanoparticles have a longer-range order, suggesting a larger particle size. Structural refinements reveal that the NFe_6 octahedra present in the Fe_3N phase at 600 °C are in fact distorted, resulting in symmetry lowering in the local structure from $P6_322$ to $P6_3$. The distortions to the NFe_6 octahedra may be caused by carbon beginning to replace N within the Fe lattice as the structure of Fe_3C consists of CFe_6 trigonal metaprisms. In summary, the study has offered us a unique insight into the mechanism of Fe_3C nanoparticle formation by sol–gel chemistry. Given that controlling the particle size is very important in metal carbide chemistry, these results suggest that focusing on the distribution of amorphous metal oxides in the precursor material will be crucial in reducing the particle size of the final carbide.

■ ASSOCIATED CONTENT

Supporting Information

The Supporting Information is available free of charge at https://pubs.acs.org/doi/10.1021/acs.inorgchem.0c03692.

Rietveld refinements of data <300 °C, PDF refinements of 350 °C samples, and structural parameters of FeO_x and Fe_3C (PDF)

■ AUTHOR INFORMATION

Corresponding Authors

Matthew S. Chambers − *School of Chemistry, University of Birmingham, Birmingham B152TT, U.K.*; Email: m.s.chambers@bham.ac.uk

Zoe Schnepp − *School of Chemistry, University of Birmingham, Birmingham B152TT, U.K.*; orcid.org/0000-0003-2171-067X; Email: z.schnepp@bham.ac.uk

Authors

Dean S. Keeble − *Diamond Light Source, Harwell Science and Innovation Campus, Didcot OX11 0DE, U.K.*

Dean Fletcher − *School of Chemistry, University of Birmingham, Birmingham B152TT, U.K.*

Joseph A. Hriljac − *School of Chemistry, University of Birmingham, Birmingham B152TT, U.K.; Diamond Light Source, Harwell Science and Innovation Campus, Didcot OX11 0DE, U.K.*; orcid.org/0000-0001-9978-6530

Complete contact information is available at: https://pubs.acs.org/10.1021/acs.inorgchem.0c03692

Author Contributions

The manuscript was written through contributions of all authors. All authors have given approval to the final version of the manuscript.

Notes

The authors declare no competing financial interest.

■ ACKNOWLEDGMENTS

The authors acknowledge the Diamond Light Source for access to beamtime on I15-1 (Proposal number EE15959) and the University of Birmingham for a postdoctoral fellowship (MSC).

■ REFERENCES

(1) Herranz, T.; Rojas, S.; Pérez-Alonso, F.; Ojeda, M.; Terreros, P.; Fierro, J. Genesis of iron carbides and their role in the synthesis of hydrocarbons from synthesis gas. *J. Catal.* **2006**, *243*, 199–211.

(2) de Smit, E.; Cinquini, F.; Beale, A. M.; Safonova, O. V.; van Beek, W.; Sautet, P.; Weckhuysen, B. M. Stability and Reactivity of

ϵ–χ–θ Iron Carbide Catalyst Phases in Fischer–Tropsch Synthesis: Controlling μC. *J. Am. Chem. Soc.* **2010**, *132*, 14928–14941.
(3) Hu, Y.; Jensen, J. O.; Zhang, W.; Cleemann, L. N.; Xing, W.; Bjerrum, N. J.; Li, Q. Hollow Spheres of Iron Carbide Nanoparticles Encased in Graphitic Layers as Oxygen Reduction Catalysts. *Angew. Chem., Int. Ed.* **2014**, *53*, 3675–3679.
(4) Feyen, M.; Weidenthaler, C.; Güttel, R.; Schlichte, K.; Holle, U.; Lu, A.-H.; Schüth, F. High-Temperature Stable, Iron-Based Core–Shell Catalysts for Ammonia Decomposition. *Chem. – Eur. J.* **2011**, *17*, 598–605.
(5) Wei, J.; Liang, Y.; Hu, Y.; Kong, B.; Simon, G. P.; Zhang, J.; Jiang, S. P.; Wang, H. A Versatile Iron–Tannin-Framework Ink Coating Strategy to Fabricate Biomass-Derived Iron Carbide/Fe-N-Carbon Catalysts for Efficient Oxygen Reduction. *Angew. Chem., Int. Ed.* **2016**, *55*, 1355–1359.
(6) Lei, L.; Zhang, L.; Gao, S.; Hu, Q.; Fang, L.; Chen, X.; Xia, Y.; Wang, X.; Ohfuji, H.; Kojima, Y.; Redfern, S. A. T.; Zeng, Z.; Chen, B.; He, D.; Irifune, T. Neutron diffraction study of the structural and magnetic properties of ϵ-$Fe_3N_{1.098}$ and ϵ-$Fe_{2.322}Co_{0.678}N_{0.888}$. *J. Alloys Compd.* **2018**, *752*, 99–105.
(7) Wang, X.; Zhu, K.; Ju, Y.; Li, Y.; Li, W.; Xu, J.; Hou, Y. Iron carbides: Magic materials with magnetic and catalytic properties. *J. Magn. Magn. Mater.* **2019**, *489*, No. 165432.
(8) Gangwar, A.; Varghese, S. S.; Meena, S. S.; Prajapat, C. L.; Gupta, N.; Prasad, N. K. Fe_3C nanoparticles for magnetic hyperthermia application. *J. Magn. Magn. Mater.* **2019**, *481*, 251–256.
(9) Fletcher, D. C.; Hunter, R.; Xia, W.; Smales, G. J.; Pauw, B. R.; Blackburn, E.; Kulak, A.; Xin, H.; Schnepp, Z. Scalable synthesis of dispersible iron carbide (Fe_3C) nanoparticles by 'nanocasting'. *J. Mater. Chem. A* **2019**, *7*, 19506–19512.
(10) Williams, B.; Clifford, D.; El-Gendy, A. A.; Carpenter, E. E. Solvothermal synthesis of Fe_7C_3 and Fe_3C nanostructures with phase and morphology control. *J. Appl. Phys.* **2016**, *120*, No. 033904.
(11) Giordano, C.; Erpen, C.; Yao, W.; Milke, B.; Antonietti, M. Metal Nitride and Metal Carbide Nanoparticles by a Soft Urea Pathway. *Chem. Mater.* **2009**, *21*, 5136–5144.
(12) Schnepp, Z.; Danks, A. E.; Hollamby, M. J.; Pauw, B. R.; Murray, C. A.; Tang, C. C. In Situ Synchrotron X-ray Diffraction Study of the Sol–Gel Synthesis of Fe_3N and Fe_3C. *Chem. Mater.* **2015**, *27*, 5094–5099.
(13) Schnepp, Z.; Thomas, M.; Glatzel, S.; Schlichte, K.; Palkovits, R.; Giordano, C. One pot route to sponge-like Fe_3N nanostructures. *J. Mater. Chem.* **2011**, *21*, 17760–17764.
(14) Bøjesen, E. D.; Iversen, B. B. The chemistry of nucleation. *CrystEngComm* **2016**, *18*, 8332–8353.
(15) Dippel, A.-C.; Jensen, K. M. O.; Tyrsted, C.; Bremholm, M.; Bojesen, E. D.; Saha, D.; Birgisson, S.; Christensen, M.; Billinge, S. J. L.; Iversen, B. B. Towards atomistic understanding of polymorphism in the solvothermal synthesis of ZrO_2 nanoparticles. *Acta Crystallogr., Sect. A: Found. Adv.* **2016**, *72*, 645–650.
(16) Stinton, G. W.; Evans, J. S. O. Parametric Rietveld refinement. *J. Appl. Crystallogr.* **2007**, *40*, 87–95.
(17) Rietveld, H. A profile refinement method for nuclear and magnetic structures. *J. Appl. Crystallogr.* **1969**, *2*, 65–71.
(18) Coelho, A. A.; Evans, J.; Evans, I.; Kern, A.; Parsons, S. The TOPAS symbolic computation system. *Powder Diffr.* **2011**, *26*, S22–S25.
(19) Fjellvåg, H.; Grønvold, F.; Stølen, S.; Hauback, B. On the Crystallographic and Magnetic Structures of Nearly Stoichiometric Iron Monoxide. *J. Solid State Chem.* **1996**, *124*, 52–57.
(20) Wood, I. G.; Vočadlo, L.; Knight, K. S.; Dobson, D. P.; Marshall, W. G.; Price, G. D.; Brodholt, J. Thermal expansion and crystal structure of cementite, Fe_3C, between 4 and 600 K determined by time-of-flight neutron powder diffraction. *J. Appl. Crystallogr.* **2004**, *37*, 82–90.
(21) Jacobs, H.; Rechenbach, D.; Zachwieja, U. Structure determination of γ'-Fe_4N and ϵ-Fe_3N. *J. Alloys Compd.* **1995**, *227*, 10–17.
(22) Coelho, A. A.; Chater, P. A.; Kern, A. Fast synthesis and refinement of the atomic pair distribution function. *J. Appl. Crystallogr.* **2015**, *48*, 869–875.
(23) Soper, A. K., *GudrunN and GudrunX: programs for correcting raw neutron and X-ray diffraction data to differential scattering cross section*. Science & Technology Facilities Council Swindon, UK: 2011.
(24) Keen, D. A comparison of various commonly used correlation functions for describing total scattering. *J. Appl. Crystallogr.* **2001**, *34*, 172–177.
(25) Lorch, E. Neutron diffraction by germania, silica and radiation-damaged silica glasses. *J. Phys. C: Solid State Phys.* **1969**, *2*, 229–237.
(26) Trucano, P.; Chen, R. Structure of graphite by neutron diffraction. *Nature* **1975**, *258*, 136–137.
(27) Yamanaka, T.; Morimoto, S. Isotope effect on anharmonic thermal atomic vibration and κ refinement of ^{12}C and ^{13}C diamond. *Acta Crystallogr., Sect. B: Struct. Sci.* **1996**, *52*, 232–238.
(28) Balzar, D.; Audebrand, N.; Daymond, M. R.; Fitch, A.; Hewat, A.; Langford, J. I.; Le Bail, A.; Louer, D.; Masson, O.; McCowan, C. N.; Popa, N. C.; Stephens, P. W.; Toby, B. H. Size-strain line-broadening analysis of the ceria round-robin sample. *J. Appl. Crystallogr.* **2004**, *37*, 911–924.
(29) Patterson, A. L. The Scherrer Formula for X-Ray Particle Size Determination. *Phys. Rev.* **1939**, *56*, 978–982.
(30) Smith, M. A.; Foley, H. C.; Lobo, R. F. A simple model describes the PDF of a non-graphitizing carbon. *Carbon* **2004**, *42*, 2041–2048.
(31) McNutt, N. W.; Rios, O.; Feygenson, M.; Proffen, T. E.; Keffer, D. J. Structural analysis of lignin-derived carbon composite anodes. *J. Appl. Crystallogr.* **2014**, *47*, 1577–1584.
(32) Cooper, S. R.; Candler, R. O.; Cosby, A. G.; Johnson, D. W.; Jensen, K. M. Ø.; Hutchison, J. E. Evolution of Atomic-Level Structure in Sub-10 Nanometer Iron Oxide Nanocrystals: Influence on Cation Occupancy and Growth Rates. *ACS Nano* **2020**, *14*, 5480–5490.
(33) Kakihana, M. Invited review "sol-gel" preparation of high temperature superconducting oxides. *J. Sol-Gel Sci. Technol.* **1996**, *6*, 7–55.
(34) Fleet, M. The structure of magnetite: two annealed natural magnetites, $Fe_{3.005}O_4$ and $Fe_{2.96}Mg_{0.04}O_4$. *Acta Crystallogr., Sect. C: Cryst. Struct. Commun.* **1984**, *40*, 1491–1493.
(35) Nakamuro, T.; Sakakibara, M.; Nada, H.; Harano, K.; Nakamura, E. Capturing the Moment of Emergence of Crystal Nucleus from Disorder. *J. Am. Chem. Soc.* **2021**, *143*, 1763–1767.
(36) Mancini, A.; Shin, J. F.; Orera, A.; Slater, P. R.; Tealdi, C.; Ren, Y.; Page, K. L.; Malavasi, L. Insight into the local structure of barium indate oxide-ion conductors: An X-ray total scattering study. *Dalton Trans.* **2012**, *41*, 50–53.
(37) Paul, T.; Tsur, Y. A protocol to detect the phase transition in $La_2Mo_2O_9$ oxide ion conductor. *Mater. Lett.* **2018**, *220*, 325–327.
(38) Danks, A. E.; Hollamby, M. J.; Hammouda, B.; Fletcher, D. C.; Johnston-Banks, F.; Rogers, S. E.; Schnepp, Z. Mechanistic insights into the formation of porous carbons from gelatin. *J. Mater. Chem. A* **2017**, *5*, 11644–11651.
(39) Dymock, K. R.; Palenik, G. J. Twist angle calculations. Fact or fantasy. *Inorg. Chem.* **1975**, *14*, 1220–1222.
(40) Flandera, M. A.; Lingafelter, E. C. Twist angle definitions. *Inorg. Chem.* **1976**, *15*, 750–750.
(41) Herbstein, F. H.; Smuts, J. Comparison of X-ray and neutron-diffraction refinements of the structure of cementite Fe_3C. *Acta Crystallogr.* **1964**, *17*, 1331–1332.
(42) du Plessis, H. E.; de Villiers, J. P. R.; Kruger, G. J.; Steuwer, A.; Brunelli, M. Rietveld and pair distribution function study of Hägg carbide using synchrotron X-ray diffraction. *J. Synchrotron Rad.* **2011**, *18*, 266–271.
(43) Jack, K. H.; Goodeve, C. F. Binary and ternary interstitial alloys - II. The iron-carbon-nitrogen system. *Proc. R. Soc. Lond. Ser. A Math. Phys. Sci.* **1948**, *195*, 41–55.

https://doi.org/10.1021/acs.inorgchem.0c03692
Inorg. Chem. 2021, 60, 7062–7069

(44) Schnepp, Z. A. C.; Wimbush, S. C.; Mann, S.; Hall, S. R. Structural Evolution of Superconductor Nanowires in Biopolymer Gels. *Adv. Mater.* **2008**, *20*, 1782−1786.

https://doi.org/10.1021/acs.inorgchem.0c03692
Inorg. Chem. 2021, 60, 7062−7069